Condition monitoring of train wheels using a cost-effective smart rail pad

Marco Heinrich van Schalkwyk (Heinvschalkwyk@gmail.com)

Petrus Johannes Gräbe (hannes.grabe@up.ac.za)

Department of Civil Engineering, University of Pretoria, Lynnwood Road, Hatfield, Pretoria 0002, South Africa.

Marco Heinrich van Schalkwyk http://orcid.org/0000-0001-8197-4920

Petrus Johannes Gräbe http://orcid.org/0000-0002-1338-6075

KEYWORDS:

Additive manufacturing

Condition monitoring

Smart materials

Wheel flats

Wheel-rail contact force

ABSTRACT:

This present paper focuses on the condition monitoring of train wheels utilizing an 3D printed rail pad that is embedded with widely available accelerometers and a strain gauge. This smart rail pad was used on a heavy haul railway line to monitor train wheels by identifying any wheel defects and measuring the respective wheel loads. A series of laboratory material tests were conducted on various 3D printing materials to identify the most suitable material for the smart rail pad. Dynamic and static loading tests were carried out to determine whether the 3D printed rail pads could withstand the typical forces exerted by a passing train. Field tests were done to determine the performance of the smart rail pads in operational conditions. Results indicated that the smart rail pads were able to identify 60 % of the wheel flats and were able to measure the wheel loads with an average percent error of 6 % by comparing it to the control measurements. In summary, the smart rail pads presented a good correlation between the measured wheel loads and the true values, while the identification of wheel flats was influenced by the low sampling rate of the system.

1 INTRODUCTION

1.1 BACKGROUND

The ballasted track is the most common track structure used worldwide due to its proven technology and ease of maintenance. With the introduction of concrete sleepers, the track structure became stiffer compared to track structures with timber sleepers. To combat the stiffer structure, elastic rail pads are placed between the rail seat and the sleeper. The function of the rail pad is to provide resiliency for the track structure and damping of wheel-induced vibrations and noise (Esveld, 2001).

The vertical stiffness of the rail pad is important for track performance and durability. Rail pads are made of various rubber and plastic materials to create rail pads with different characteristics and mechanical behaviour. Various 3D printing plastics could provide similar performance and durability compared to regular rail pads. Three 3D printing materials were tested in this study including Polylactic Acid (PLA), Polyethylene Terephthalate modified with Glycol (PETG) and Thermoplastic Polyurethane (TPU). PLA and PETG were used because they are affordable and readily available. Recent studies have applied PLA, PETG and TPU to various applications because of their specific properties (Hong et al., 2019; Wang et al., 2020; Lee et al., 2019). TPU was used due to its high flexibility, elasticity and impact resistance (Lee et al., 2019). With the onset of 3D printing technology, a new and interesting method of creating rail pads can be introduced.

Sensing instrumentation plays an important role in measuring both the performance and the condition of the railway track. Data on how the various components of a railway track respond to a passing train in terms of acceleration, vibration, displacement and loading are necessary for condition monitoring of the railway track. Various trackside monitoring instrumentation such as Linear Variable Differential Transducers (LVDTs), accelerometers, geophones and stain gauges have been shown to provide these measurements, however, they are primarily research equipment that are costly and practical deployments are narrow in scope (Milne et al., 2016). To thoroughly evaluate the structural condition of the railway track, new cost-effective approaches to condition monitoring are required.

Smart rail pads are a new concept that has only been researched and developed to a limited extent. Measurements from inside the rail pad can be obtained by the installation of instruments such as Micro-Electro-Mechanical System (MEMS) accelerometers

(Milne et al., 2016; Stenström et al., 2019), piezoelectric sensors (Zhang et al., 2018; Sol-Sánchez et al., 2021a) and fibre optics (Woschitz, 2011; Zhang et al., 2014). Operational parameters such as accelerations, vibrations, axle load, frequency and temperature can be measured using sensing instrumentation installed inside a rail pad and these measurements could enable condition monitoring of the track structure.

The previous literature and research (Zhang et al., 2018; Sol-Sánchez et al., 2021a; Woschitz, 2011; Zhang et al., 2014) on smart rail pads provided evidence that it is possible to produce a condition monitoring system by installing sensing instrumentation inside a track component such as a rail pad. To date, no smart rail pad has been created that incorporates both accelerometer and strain gauge technology. Previous research did not consider the possibility of fabricating a low-cost remote monitoring system that automatically detects an oncoming train and captures data from instrumentation inside a smart rail pad. Fabricating a rail pad from 3D printing filament is unexplored and can provide an exciting avenue for new possibilities. The objective of this study was to investigate the effectiveness of smart sensing technology, fitted inside a 3D printed rail pad, to monitor the condition of train wheels. Particularly, this work focused on investigating the effectiveness of 3D printing technology for generating a rail pad. This study therefore focused on embedding accelerometers inside the rail pad to provide monitoring of wheel defects when high impact forces occur. Load sensing capabilities using strain gauges can measure the wheel load at the rail seat area which provides an insight into the wheel load distribution from the rail to the sleepers. Calibrating the smart rail pad to field conditions can allow for direct wheel load measurement. Creating a measuring enclosure that is mounted to the rail to allow the ability for remote monitoring by detecting an oncoming train and switching the system on is also investigated. Thus, this paper aims to quantify the dynamic response of a smart rail pad using embedded sensing technology, in both laboratory and field environments.

2 DESIGN OF A 3D PRINTED SMART RAIL PAD

2.1 MATERIAL TESTING

This section covers the material testing that was conducted on the three chosen 3D printing filaments namely PLA, PETG and TPU. The material testing was done according to the ASTM standards D638 and D695 for tensile and compressive plastic material testing, respectively (ASTM, 2014; ASTM, 2015).

2.1.1 Tensile and Compressive Strength

According to the ASTM D638, a dog bone-shaped specimen is used to test the tensile strength of plastics (ASTM, 2014). The specified specimen shapes are the following: Type I for rigid plastics and Type IV for nonrigid plastics, as displayed in Figure 1. For testing purposes, five specimens of each of the three filaments at four different infill percentages (25 %, 50 %, 75 % and 100 %), with the “line” infill pattern, were tested with a total of 60 specimens.

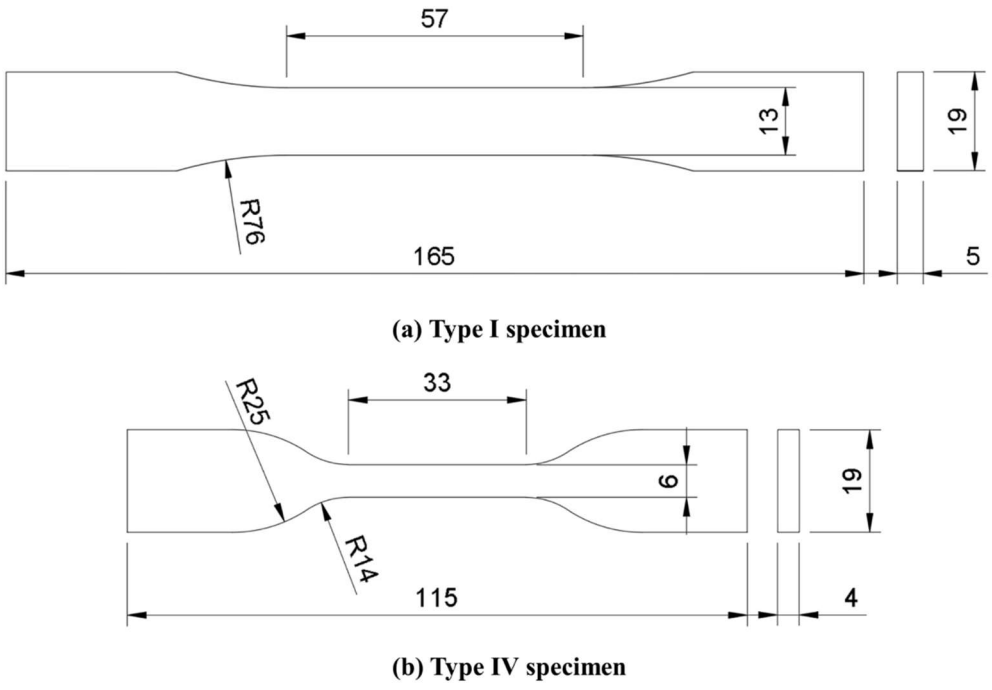

Figure 1: Dimensions (in mm) according to ASTM D638. (a) Type I and (b) Type IV specimen (ASTM, 2014)

According to ASTM D695, a standard-sized prism of 12.7 × 12.7 × 25.4 mm is used to test the compressive strength of rigid plastics (ASTM, 2015). The testing for the tensile

and compressive strength was done on Lloyd testing machines with a force range of 5 kN and 50 kN, respectively.

2.1.2 Full-scale Test Prints

The full-scale 3D printed rail pads were made in a rectangular shape of 168 mm × 175 mm × 10 mm (width × length × thickness). The rail pad thickness was chosen as 10 mm to provide enough support above and below the instrumentation. These dimensions are similar to a High-Density Polyethylene (HDPE) rail pad that was replaced in the field experiment. HDPE rail pads were first introduced in the 1970s, replacing rubber pads to provide more durability, stability and longer service life. A simple rectangular design provided optimal space for the instrumentation and shortened the printing time required. Table 1 provides detail on the physical characteristics of the tested materials.

Table 1: Physical characteristics of PLA, PETG and TPU

Material	Tensile Strength (MPa)	Compressive Strength (MPa)	Tensile Elastic Modulus (GPa)	Compression Elastic Modulus (GPa)
PLA	31.3	54.0	5.2	1.4
PETG	25.6	40.4	1.9	0.9
TPU	27.4	N/A	18.6 (*MPa*)	N/A

The pads were printed using a 0.4 mm extruder nozzle on a CReality CR-6 printer. The printing speeds varied greatly due to the different levels of difficulty in printing each filament and in particular TPU. TPU is a flexible filament and requires a slower printing speed to allow for the filament to extrude through the nozzle. It must be printed on a small printer because the length of the feeding tube can cause problems. The overall print time for TPU was not feasible for printing prototypes or even for a small amount of TPU rail pads.

2.1.3 Load Testing of full-scale prints

Cyclic testing was performed to determine whether the 3D printed rail pads could withstand the dynamic forces of an existing railway line. The rail pads tested under cyclic loading were the 3D printed pads as well as an HDPE and a Hytrel pad. Figure 2 displays the various pads that were tested with the sizing of each.

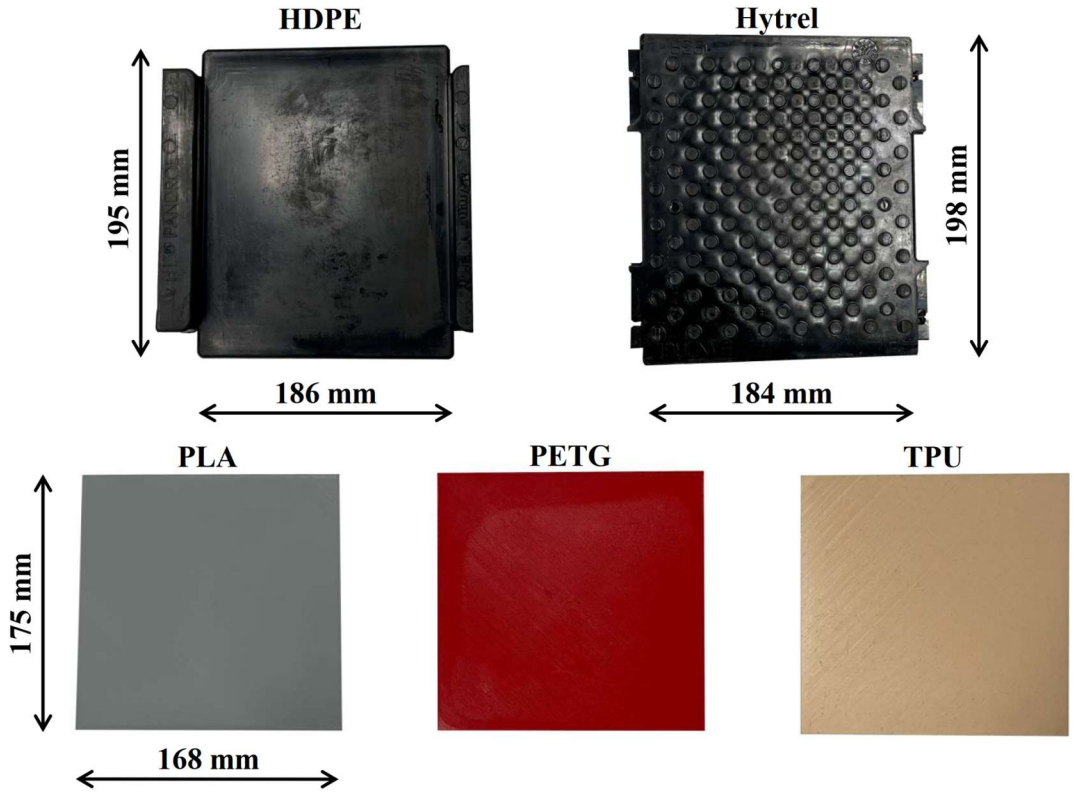

Figure 2: Types and dimensions of the pads that were tested

The cyclic tests were performed on an MTS (Materials Testing System) hydraulic actuator. The actuator has a force capacity of 500 kN for both compression and tension. The experimental setup consisted of a half-track structure that could be used in this way due to its longitudinal track symmetry. A 60 kg/m rail was placed on top of the pad and fastened down with e-clips. The track structure was not placed inside a ballast box to mitigate the damping that the ballast would provide. This decision was taken to simulate higher forces than those of an existing track structure. The experimental setup is displayed in Figure 3.

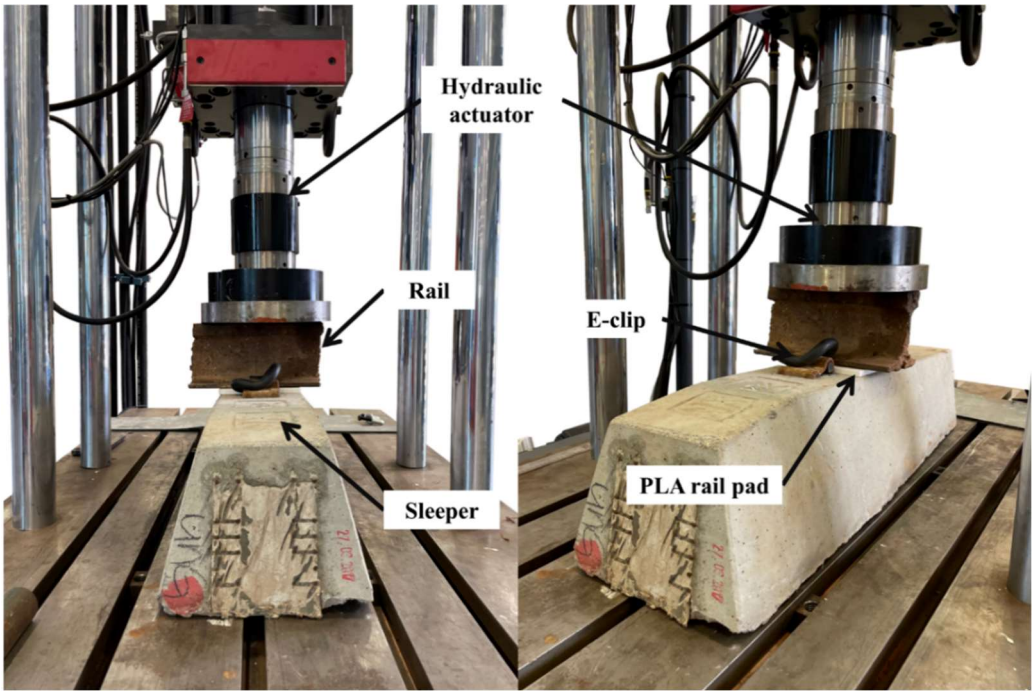

Figure 3: Hydraulic actuator and experimental components

The magnitude for the cyclic and static loading was the maximum rail seat load of 60 kN for general freight and passenger trains. The chosen load distribution percentage of 45 % for the sleeper directly below the wheel was based on the findings of Russel et al. (2020) and Profillidis (2000). The maximum rail seat load includes a dynamic impact factor according to the Eisenmann (1972) approach.

The cyclic testing frequency was determined using the equation below in a sinusoidal pattern. A sinusoidal vibration wave is generated with a frequency f when a wavelength λ is present on the rail and travels at a speed V written as (Thompson, 2009):

$$f = \frac{V}{\lambda} \qquad \text{(Equation 1)}$$

The frequency is in Hz where λ is given in m and V in m/s. The cyclic loading was applied at a frequency of 25 Hz. A vehicle speed of 165 km/h corresponds to the frequency of 25 Hz that is experienced by the rail. A wavelength of 1.83 m was used which is the axle distance of a CR-13 or CCR-11 coal wagon on the heavy haul line in South Africa. Heavy haul lines operate at low speeds (typically 50 – 80 km/h on average). According to Aursudkij et al. (2009), the typical loading frequency is between 8 – 10 Hz (assuming a train speed of 75 - 94 km/h and an axle spacing of 2.6 m) and up to 30 Hz for high-speed trains. The testing frequency of 25 Hz therefore simulates high frequencies that can occur on an existing railway line due to wheel flats and vehicle or

track irregularities. The cyclic test procedure is illustrated in Figure 4. A pre-load of 2 kN was applied from which the static test started to evenly apply 60 kN on the rail. After the static test, cyclic testing of 100,000 cycles was repeated five times for a total of 500,000 cycles.

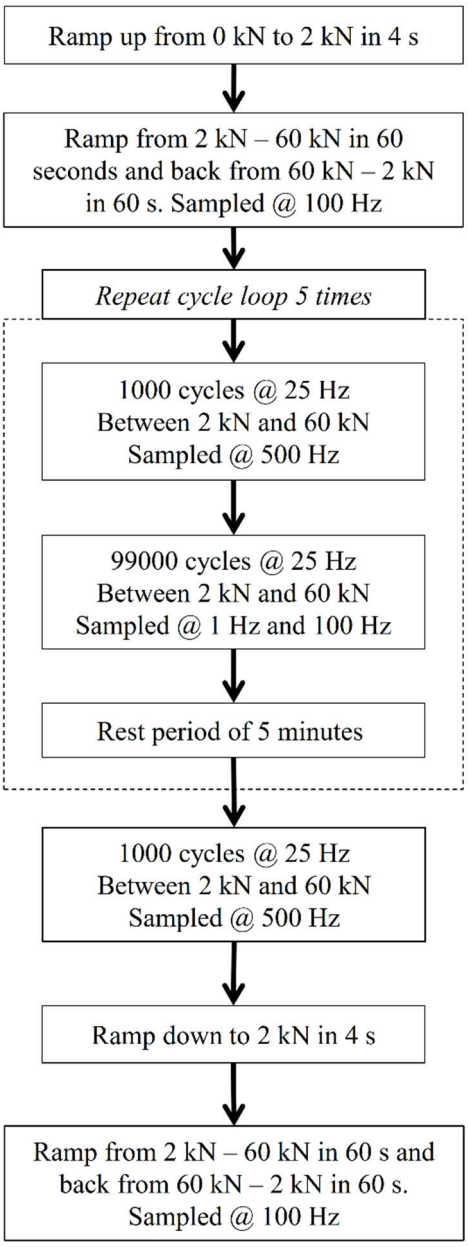

Figure 4: Cyclic testing procedure

Five individual static tests were also conducted on each test pad. The static loading consisted of a pre-load of 2 kN with an increasing load from 2 – 60 kN in 60 s and unloading back to 2 kN in another 60 s.

2.2 PROTOTYPE TESTING

The initial prototype testing was done with an inexpensive accelerometer (ADXL 335) to determine whether the PETG rail pad can protect an accelerometer embedded inside the rail pad while cyclic loading is applied. The strain prototype included an XY-1 Rosette strain gauge that was configured as a Wheatstone half-bridge. The final design would incorporate two accelerometers that can measure greater accelerations experienced inside a rail pad.

2.2.1 Accelerometer Prototype

The prototype was printed from PETG filament with the same printing settings as the full-scale test prints. The accessibility of embedding the accelerometer in the rail pad was enhanced by the ability to pause the printer (Hong et al., 2019). The printer retained the temperature of the extruder and the print bed at the correct temperature and could continue printing at any moment. Once the printer was paused, the extruder moved to the edge of the print bed which allowed for the installation of the accelerometer.

The prototype was tested on a hydraulic actuator for 1000 cycles at eight different frequencies with an applied maximum rail seat load, q_r of 86 kN. The maximum load was increased for heavy haul freight with an axle load of 26 ton/axle and included the dynamic load factor according to the Eisenmann (1972) approach. Priest et al. (2010) stated that the following loading frequencies by pairs of bogies at the ends of adjacent wagons (1 Hz), individual bogies (2 Hz) and axles (6 Hz) are apparent on a railway line. The other frequencies (8 – 25 Hz) were included to simulate the higher frequencies that could occur on a railway line due to wheel flats or rail and wagon irregularities. An external HBM WI/10 mm LVDT was placed on the rail with the reference to the sleeper to measure the rail pad deflection.

2.3 FINAL DESIGN

2.3.1 Instrumentation

The prototyping phase was used to determine whether the 3D printed rail pad would withstand the typical forces of an existing rail pad without damage to the sensors inside. The risk of sensor damage was mitigated by using the ADXL335 accelerometer in the prototyping phase. The accelerometer was changed between the prototype (ADXL335) and the final design (LIS331) because the final design required a digital accelerometer, of which the ADXL335 is an analog accelerometer, to connect two of them on a single

I2C connection for ease of use and simplicity. The accelerometer characteristics is shown in Table 2. The chosen strain gauge was the 120 Ω XY-1 Rosette which can easily be used in a half-bridge configuration. Two 120 Ω precision resistors were used for the completion circuit that was built into the external measuring enclosure. The strain gauge was configured in a Wheatstone half-bridge to increase the sensitivity of the strain gauge, while compensating for temperature changes that could have an undesired effect.

Table 2: Accelerometer characteristics

Accelerometer	Full-scale measurement range (g)	Sensitivity
LIS331	±6, ±12, ±24	3, 6, 12 mg/digit
ADXL335	±3	300 mV/g

2.3.2 Embedding process

The embedding process for the final design was similar to both prototypes with only minor additions. The rail pad was 3D modelled to have pre-designed cavities and channels for the instrumentation. The 3D printer was paused at 50 % printing process to allow for the installation of the sensors. After the sensors were installed, the printer was allowed to continue printing and encapsulate the sensors forming one solid 3D printed rail pad. Two identical PETG rail pads were made, one black (Pad 1) in colour and another one grey (Pad 2). Figure 5 (a) and (b) show the instrumentation embedded in smart Pads 1 and 2, respectively.

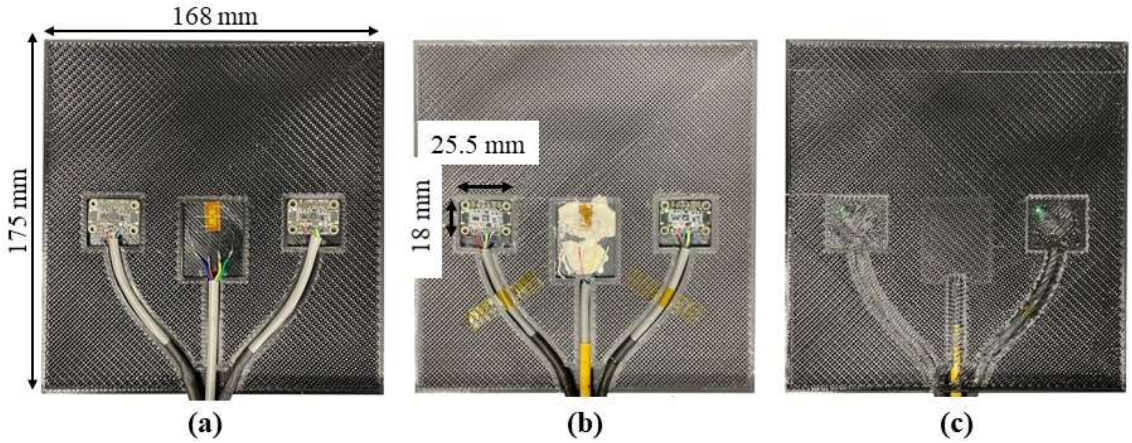

Figure 5: Embedding process for final smart rail pads: (a) two LIS331 accelerometers and the XY-1 strain gauge, (b) embedded instrumentation for smart Pad 2 and (c) first printed top layer on Pad 1

2.3.3 External measuring enclosure

The external measuring box housed the microcontroller (Razor), external strain gauge completion circuit, ADC and the battery, shown in Figure 6. The measuring enclosure was mounted to the rail with two magnets with a pull strength of 4 kg each. The Razor was fixed to the enclosure with standoffs that lift the Razor 10 mm in the air. This was done to minimise the magnetic interference that could affect the Razor measurements. All external wiring from the smart rail pad to the measuring enclosure was a 4-core shielded cable to mitigate any electrical interference that could cause problems when subjected to field conditions. The MCP3424 ADC is a part of the external circuit and converts the voltage signal from the strain gauge into a digital reading. The ADC connects to the Razor through the I^2C interface similar to the accelerometers. The resolution of the ADC can be set to 12, 14, 16, or 18-bit with corresponding sampling rates of 240, 60, 15 and 3.75 Hz, respectively. For the final design, a resolution of 14-bit was chosen to have enough sensitivity, while still sampling at a high enough frequency. A programmable gain amplifier in the ADC allows the amplification of weaker voltage signals.

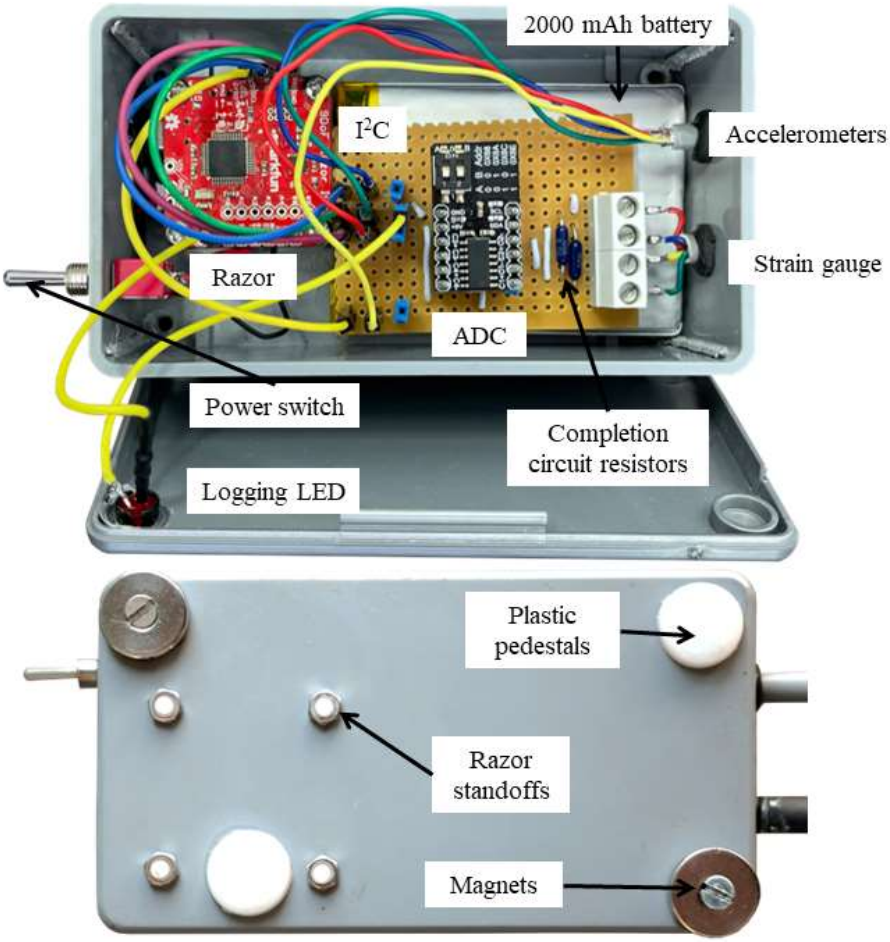

Figure 6: External measuring enclosure, top and bottom view

The final sampling frequency of the smart rail pad was 40 Hz. The low sampling rate is due to two factors; (1) the ADC responsible for the voltage conversions and (2) the amount of instrumentation and axes that needed to be logged. The low sampling rate is not ideal, but it was still high enough for sufficient information. The highest frequency component of interest, present in the field experiment, was between 8-10 Hz for the axles of the wagons. Theoretically, the sampling rate of 40 Hz is sufficient to sample the signal emanating from the axles.

3 EXPERIMENTAL SETUP

3.1 FIELD EXPERIMENT

The field experiment was conducted on the Ermelo-Richards Bay coal line, at the test site called “Bloubank” situated 60 km from Vryheid, KwaZulu-Natal in South Africa. Details of the specification for the heavy haul line is given by Gräbe et al. (2005):

- Track gauge: 1065 mm
- Sleepers: FY concrete (to accommodate Fist fasteners)
- Axle load: 26 ton/axle
- Sleeper spacing: 650 mm
- Fastening system: Fist fasteners
- Electrified

The field setup was done on Line 1 of the double line track where the loaded trains travel from northwest to southeast (increasing kilometres). The track alignment consisted of a curve with a tangent section, passing the test site, before entering a tunnel. Figure 7 shows the locality map of the test site and the selected section of track, where the smart rail pads were installed. The selected section was chosen because it had a good quality ballast layer that would not have any excessive deformation as well as being close enough to electricity supply. The mast pole served as a good infrastructure reference point.

The crib ballast from six sleepers had to be moved away, three on each side of the chosen sleeper. This had to be done before the Fist fasteners could be removed in order to lift the rail. After the rail was lifted with a hydraulic jack, two smart rail pads were installed on either side of the sleeper. The replacement process is displayed in Figure 8.

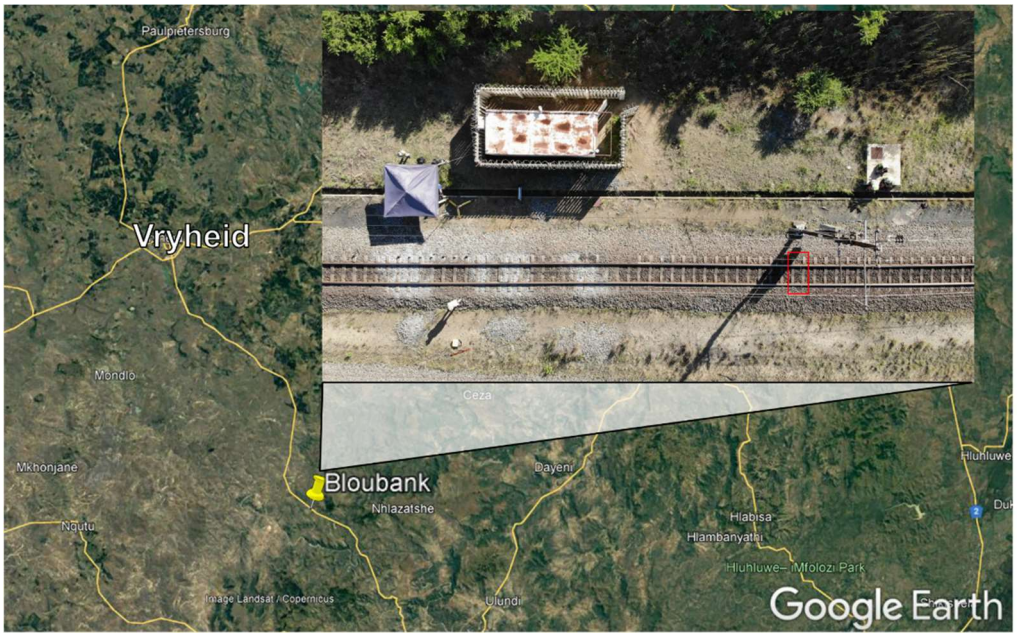

Figure 7: Field experiment location map (the testing site displayed with the red box)

Figure 8: Rail pad replacement: (a) opening made for removing Fist fasteners, (b) process of removing Fist fasteners, (c) hydraulic jack to lift the rail and (d) the installation of the smart rail pad

Control measurements were taken to validate the performance of the smart rail pads. Four vertical strain gauges were installed on each rail for wheel load measurements. The rust on the rail was grinded away before the strain gauges were glued to the rail to ensure a clean bond between the two. The strain gauges were fastened to the rail with X60 glue. Five LVDTs were installed to measure pad deflection. Four LVDTs were placed on the chosen sleeper, to validate the pad deflection of the smart rail pads, with another LVDT measuring the pad deflection of a normal HDPE pad on a different sleeper. Figure 9 displays the installation of the control instrumentation. The LVDTs were mounted to the rail with magnetic rods and was held in place with a steel clamp. The position of the LVDTs were such that the relative deflection difference between the rail and the sleeper could be measured, which would be equal to the pad deflection. The measuring enclosure was placed inside a plastic bag to protect the magnets from steel fibres and to protect the electronics from moisture. A cross-section diagram of the experimental setup can be seen in Figure 10.

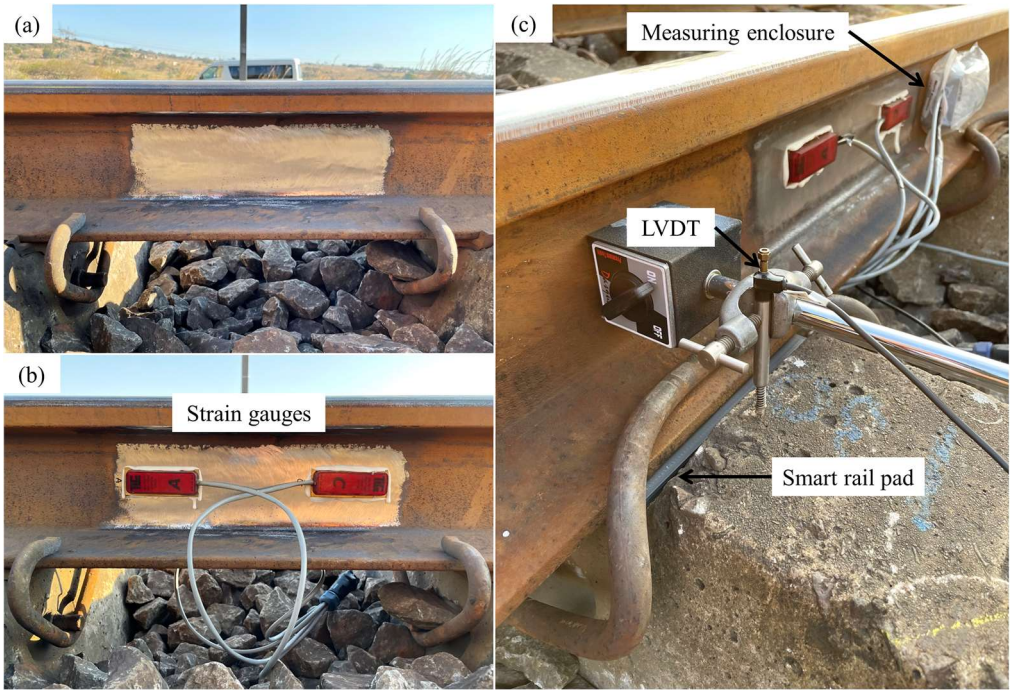

Figure 9: Installation of control instrumentation: (a) grinded rail, (b) glued strain gauges and (c) LVDT clamped onto the magnetic rod

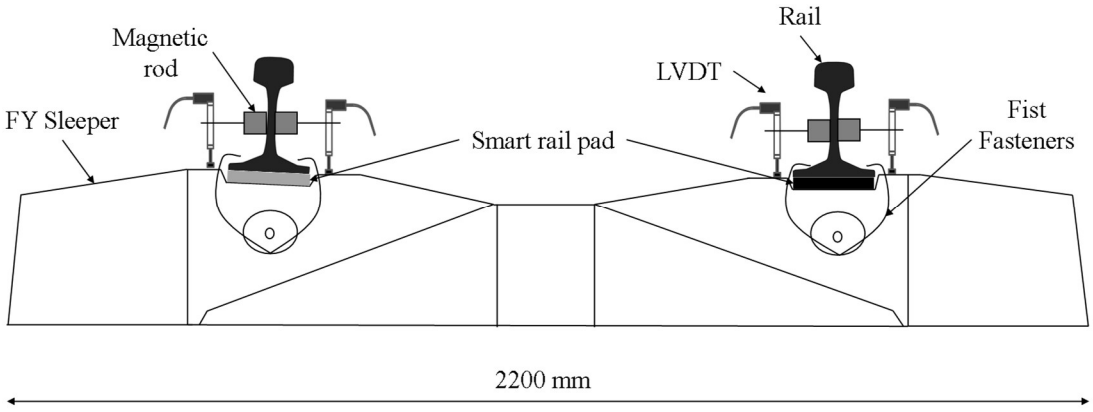

Figure 10: Cross-section diagram of the field test setup with the grey and black PETG pads situated on the left and right, respectively

Six trains in total, were logged with both the smart rail pads and the control instrumentation. Various locomotive and wagon types were captured. The smart rail pads were left overnight to test the automatic triggering and the battery life of the system. The maximum runtime of the system was 42 hours with a 2000 mAh battery while logging all the instrumentation, which was sufficient for short-term testing. Automatic triggering was added to the system with a threshold value that was determined in the laboratory and checked in the field for passing trains. The threshold value was changed according to field conditions after the initial passing trains so that it could trigger correctly for any future trains. The automatic triggering allowed the rail pads to respectively measure six trains during the night. This provided evidence of the effectiveness of the automatic triggering of the Razor to log the data from the instrumentation inside the smart rail pad. The automatic triggering allowed for continuous condition monitoring of the train wheels.

4 ANALYSIS AND DISCUSSION

4.1 3D PRINTED RAIL PAD

The 3D printing material was not only characterised by the results from the tensile and compression testing, but was also tested in a 3D printed rail pad form. The 3D printed rail pad was tested on a hydraulic actuator for 500,000 cycles to determine whether the material would deform significantly under realistic vertical loading.

4.1.1 Static Stiffness

The loading and unloading of the rail pads in the static test at the end of the 500,000 cycles is shown in Figure 11. All the rail pads, except TPU, has an elastic loading and unloading curve, where the curves start and end at the same deformation, suggesting no plastic deformation. The opposite is true for TPU, which displayed a plastic deformation of 0.56 mm. There was minor hysteresis for PETG, PLA and HDPE. The TPU pad exhibited the greatest extent of hysteresis for an elastic loading and unloading curve. Hysteresis, i.e., the divergence of the two paths, shows the amount of energy loss in the form of heat between the two loading phases.

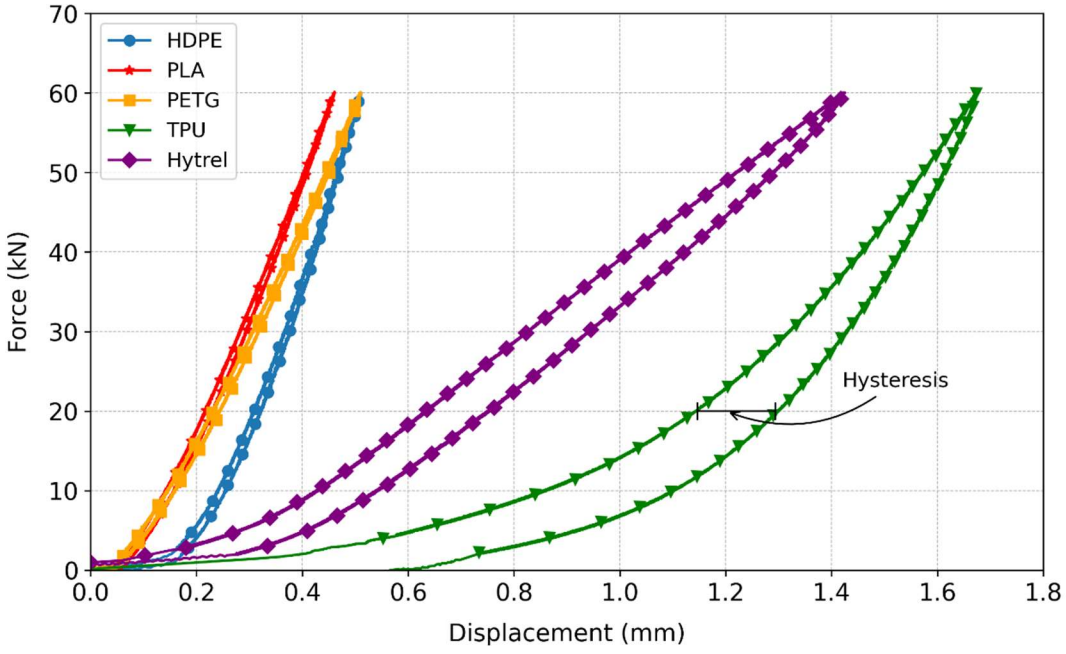

Figure 11: Loading and unloading curves for each tested rail pad

4.1.2 Dynamic Stiffness

The main purpose of the dynamic testing was to determine whether a 3D printed rail pad could sustain the typical forces that a real rail pad experiences without excessive plastic deformation. The dynamic stiffness of the first 1000 cycles of every 100,000 cycles was calculated, as well as that of the last 1000 cycles at the end of the test. The dynamic stiffness of each rail pad is displayed in Figure 12. The dynamic stiffness rapidly increased for each rail pad as the cycles increased. The rail pads stiffened to an extent as loads were applied to it. The results of the dynamic stiffness of the three 3D printed rail pads are located between that of the two manufactured (HDPE and Hytrel) control pads. PLA is stronger and stiffer than PETG. A requirement for a 3D printed rail pad was that it needed to provide support for the internal instrumentation, while still providing the elasticity of a rail pad. The natural first choice would have been PLA because it is the strongest of the three filaments. However, PETG is strong enough to support the internal instrumentation and provide some elasticity when in the form of a rail pad. The decision was made to use PETG because of its strength to protect internal instrumentation while providing elasticity to the track structure. It also has a greater glass transition temperature, meaning that it will perform better in hot climates and not deform due to high temperature, compared to PLA.

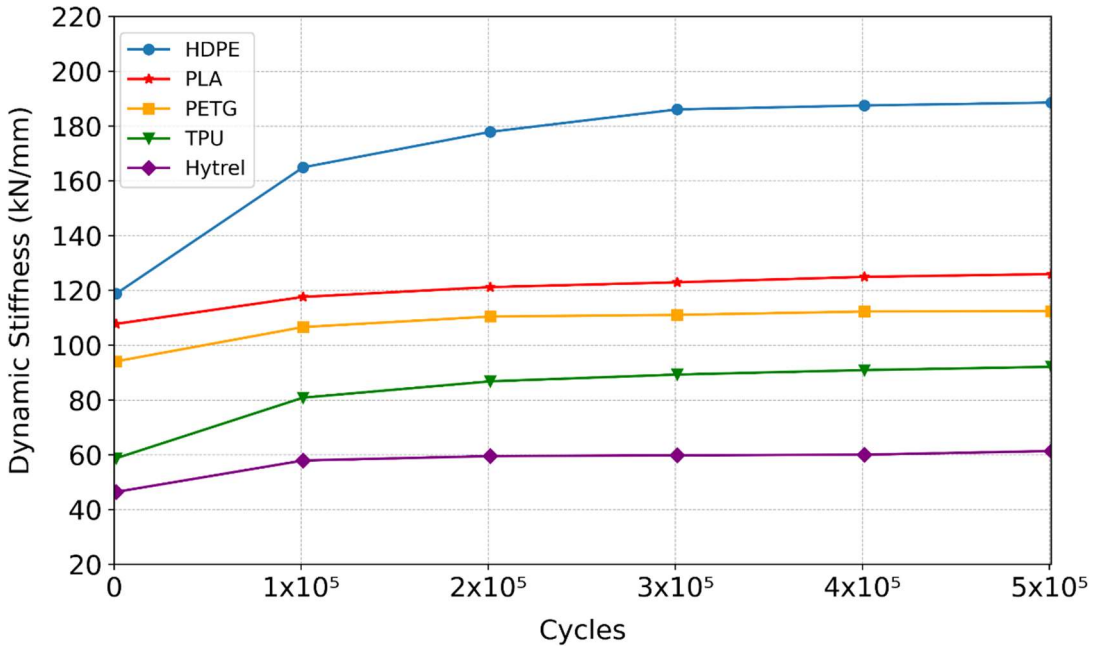

Figure 12: Dynamic stiffness of each rail pad during 500,000 loading cycles

4.2 PROTOTYPE TESTING

4.2.1 Accelerometer Prototype

The accelerometer prototype housed an ADXL335 accelerometer and was logged with an Arduino Mega. The cyclic testing consisted of 1000 cycles at various frequencies to simulate trains and axles travelling at different speeds. An LVDT was used as the control measurement to verify the displacements obtained from the double integrated accelerations of the accelerometer. The comparison was done to ascertain whether the accelerometer could accurately determine the pad deflection. Pre-processing of each tested frequency was done before analysing the data. The accelerations of the tested frequencies: 1, 2, 6, 8, 10, 15, 20 and 25 Hz were filtered with a 4th order bandpass Butterworth filter around each frequency magnitude. Thereafter, the filtered accelerations were integrated twice, using the trapezoidal rule, to calculate displacements with a first-order trend removal at the end of the process to compensate for the cumulative nature of the integration.

The descriptive statistics related to the mean, standard deviation, minimum and maximum were evaluated and compared for the LVDT and the accelerometer prototype. Any outliers, for both the minimum and maximum measurements, were removed before peak detection. The peak detection method identifies a maximum point when it has a maximal value and was preceded (to the left) by a value lower than the threshold value (Billauer, 2010). To compare the results, the mean peak-to-peak displacement was calculated to provide an average characteristic displacement for each instrument (Milne et al., 2016). The frequencies of 1 Hz and 2 Hz were omitted because their mean, maximum and standard deviation values, were too large to display with the other values. The peak-to-peak mean difference between the accelerometer and the LVDT was 4.42 mm and 0.91 mm, for 1 Hz and 2 Hz respectively. Considerably small accelerations were measured for the frequencies of 1 Hz and 2 Hz. It was noted by Milne et al. (2016) that this is a performance limitation of the sensor. To this end, the displacements were overestimated by the integration of the small accelerations resulting in unrealistic displacements. This must be considered since it could limit the detection of minor track variations and only be suitable for significant changes in track performance such as hanging sleepers and high-impact wheel flats (Sol-Sánchez et al., 2021b). Figure 13 displays the mean displacement difference between the LVDT and the accelerometer data across the tested frequencies.

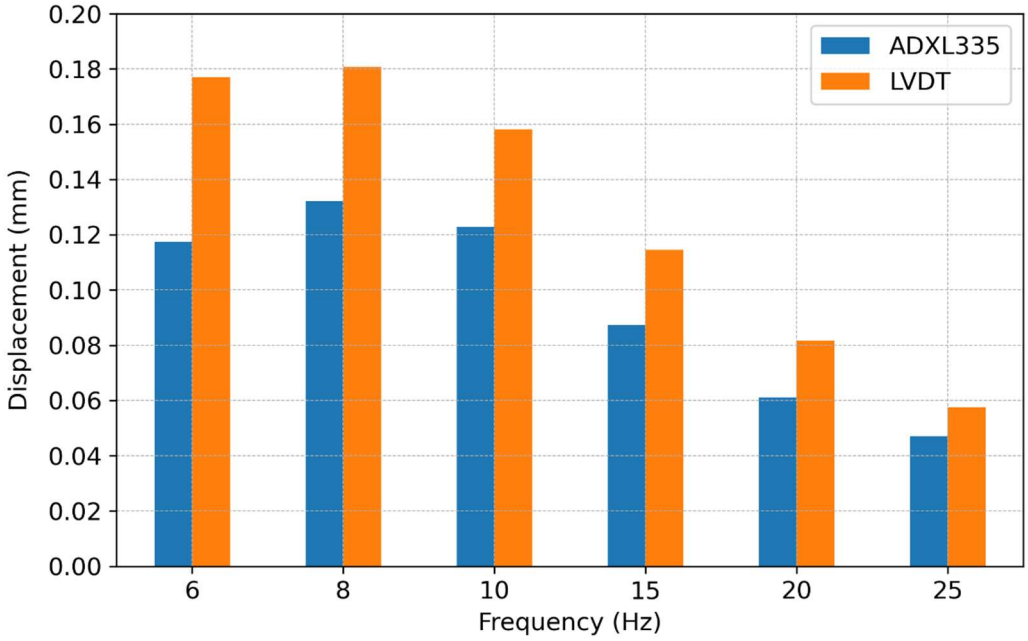

Figure 13: Mean peak-to-peak displacements from the accelerometer and LVDT

The rail pad deflection was underestimated across all frequencies by the integrated displacements from the accelerometer data when compared to the LVDT measurements. The degree of underestimation decreases as the frequency increases, which agrees with that of Milne et al. (2016). This is in part due to the large standard deviation of the integrated displacements that decreases the mean value. The mean difference between the two decreases as the frequency increases. As the frequency increases, the magnitude of the displacements decreases, for both instruments.

4.3 SMART RAIL PAD

4.3.1 Identification of wheel defects in the field

The two identical PETG smart rail pads were installed on opposite ends of the same sleeper at the Bloubank test site. Two LVDTs for each smart pad were installed as the control measurement for the rail pad deflection and wheel defect detection. The acceleration data from the smart rail pad was integrated twice, using the trapezoidal rule with a 1 Hz high pass Butterworth filter, for displacement. Thereafter, a mean filter with a window size of three, was used to remove the trend/drift that occurs when double integrating acceleration to displacement. Due to the low sampling rate of 40 Hz, no filtering of the data was required for the removal of any high frequencies. Figure 14

illustrates an example deflection bowl in the field test of the left accelerometer in the grey pad compared to the LVDT on the left field side of the track structure.

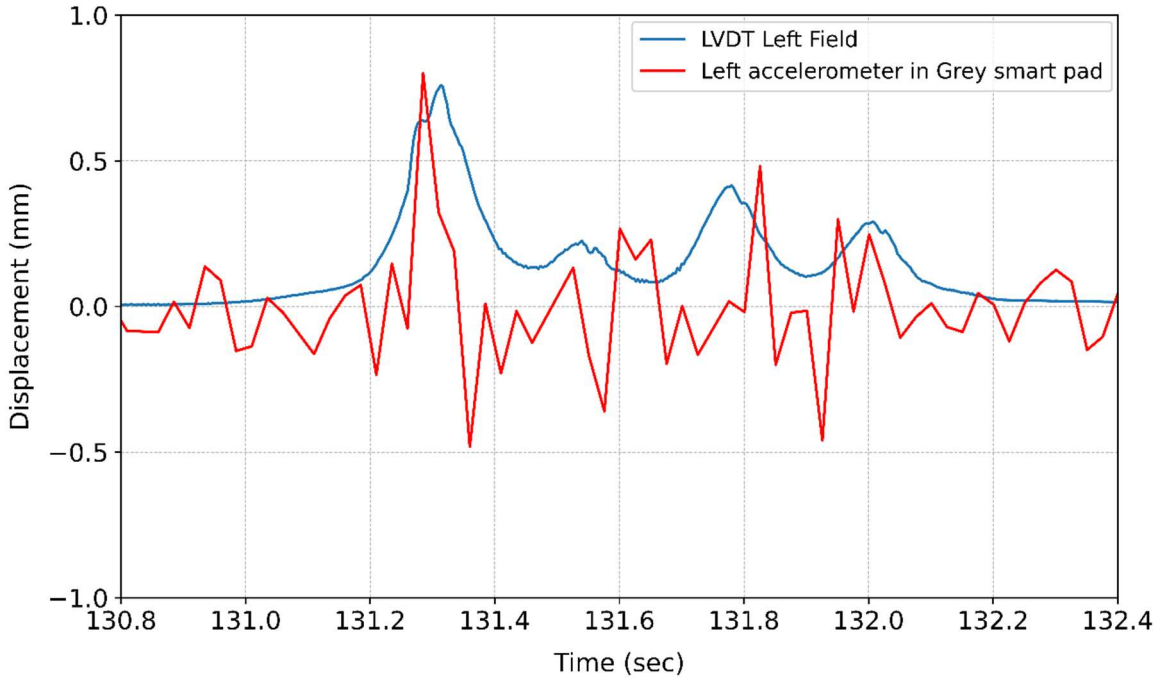

Figure 14: Left Accelerometer in smart pad compared with the left field LVDT

The wheel defects (characterised as high dynamic impact forces with associated high frequencies), which were identified by the LVDT data, was used as a control to compare whether the smart pad was able to successfully identify the same defects. The position and the magnitude of the wheel defects, between the LVDTs and the smart pads, were compared. This was done to ascertain the success factor to which the smart rail pads identified any wheel defects. The smart rail pads missed some wheel defects where it did not create a large enough displacement or event to classify it as a wheel defect when compared to the LVDT displacement. This was due to the limitation of the 40 Hz sample rate and the 3D loading of the wheel on the rail. The smart rail pads also had false readings of wheel defects where other external elements such as rolling stock movement and a wide range of excited external frequencies created large displacement readings for the smart rail pads and not for the LVDTs.

The average displacement of each train was used as an indication to distinguish between a normal wheel and a defective wheel. The defective wheels were taken as any pad displacement above 0.5 mm, whereas any displacement below that was classified as

normal. A wheel defect was only successfully identified when it had a distinct peak and/or shape or a big disturbance/event in the accelerometer displacement data and was above 0.5 mm. Some of the peak displacements from the LVDTs were under- or overestimated by the accelerometers, however, it still had a clear indication that it was a wheel defect. Figure 15 displays the percentage of successfully identified wheel defects for both the smart rail pads.

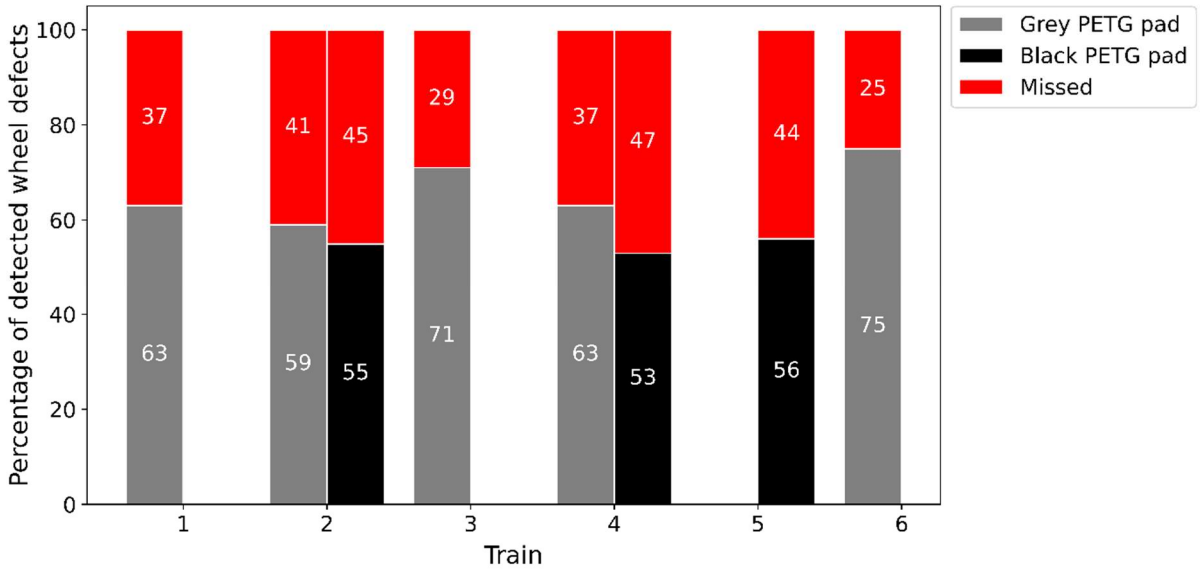

Figure 15: Successfully identified wheel defects from both smart rail pads

The results were normalised to a percentage of the true wheel defects from the LVDTs that were identified by the smart rail pads. The grey and black bars indicate the successfully identified wheel defects for each smart rail pad and the red bars indicate the missed wheel defects. The number of successfully detected wheel defects were relatively constant across all the trains for the grey and black smart rail pads. The level of accuracy was not high due to the limiting sampling rate of 40 Hz, the other external frequencies that could influence the readings and the type of loading that the rail pad experienced in the field. All the successfully detected wheel defect percentages, for the grey and black smart rail pads, were above 50 %, proving that wheel defects can be detected to an acceptable extent by using accelerometers and the strain gauge inside the smart rail pad.

4.3.2 Load Sensing Capabilities

The main purpose of the strain gauge in the smart rail pad was to be used as the load sensing instrument. The strain gauge in the smart rail pad was calibrated according to the field conditions using the control strain gauges that were glued to the rail. A calibration factor of 1.98 mV/ton or 0.2 mV/kN with a coefficient of determination (R^2) for the linear fit of 0.991 was determined. The calibration was done on the known mass of the locomotives in front of each train. The calibration factor was used to convert the mV signals from the smart rail pad to tons for the approximated wheel load. The calibrated signal response from the grey smart pad, below the left rail, compared with the control strain gauge is illustrated in Figure 16. The smart rail pad also showed excellent signal response to the variation in loading magnitude of the tested trains and could therefore successfully be used to measure the wheel loads. The calibrated wheel loads from the smart rail pad were in close agreement with the true value of the wheel loads from the control strain gauges.

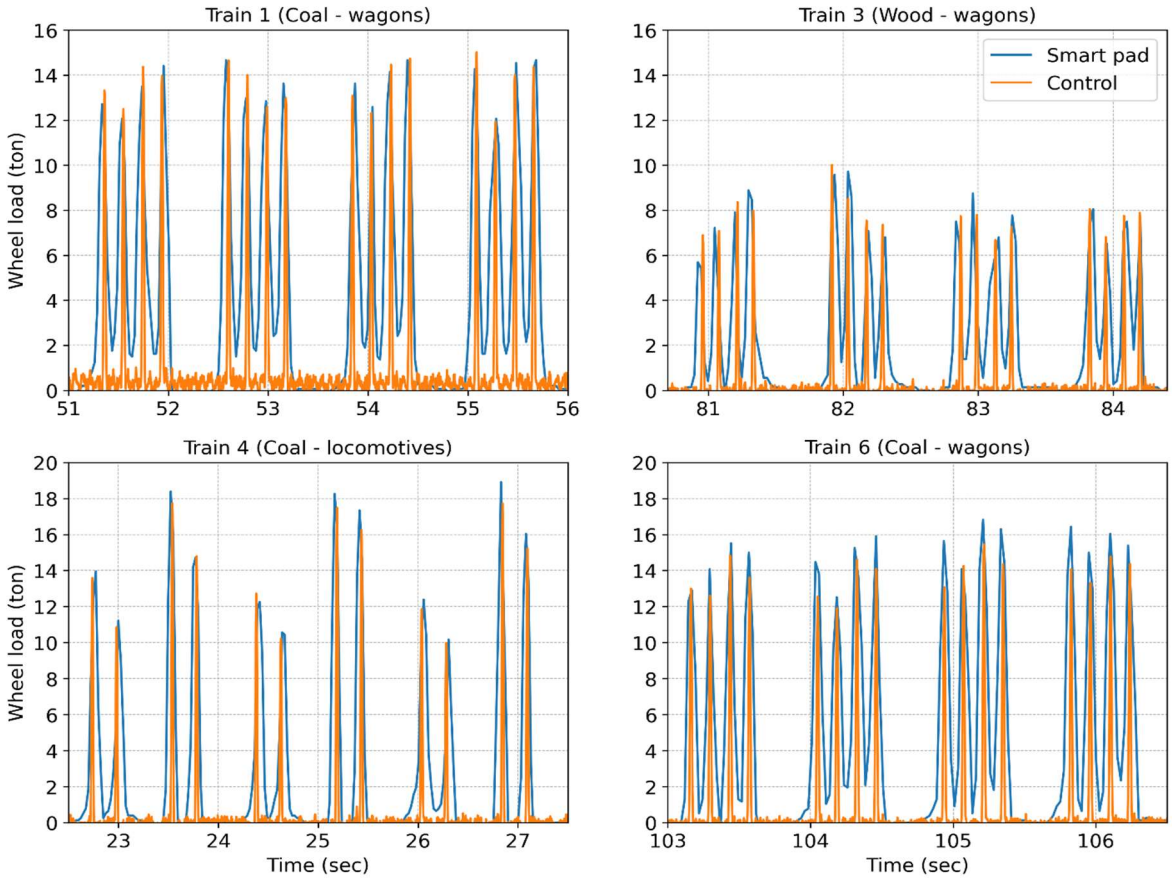

Figure 16: Wheel loads from the grey PETG smart rail pad compared to the true value for Trains 1, 3, 4 and 6

Figure 17 illustrates the linear relationship between the measured wheel loads and the true value of the wheel loads of 2676 train wheels. The linear relationship has a coefficient of determination (R^2) for the linear fit of 0.868 proving that the smart rail pad displays a good correlation between the measured and the true wheel loads. These results demonstrate that the smart rail pad could be used as an axle counter and to measure wheel loads.

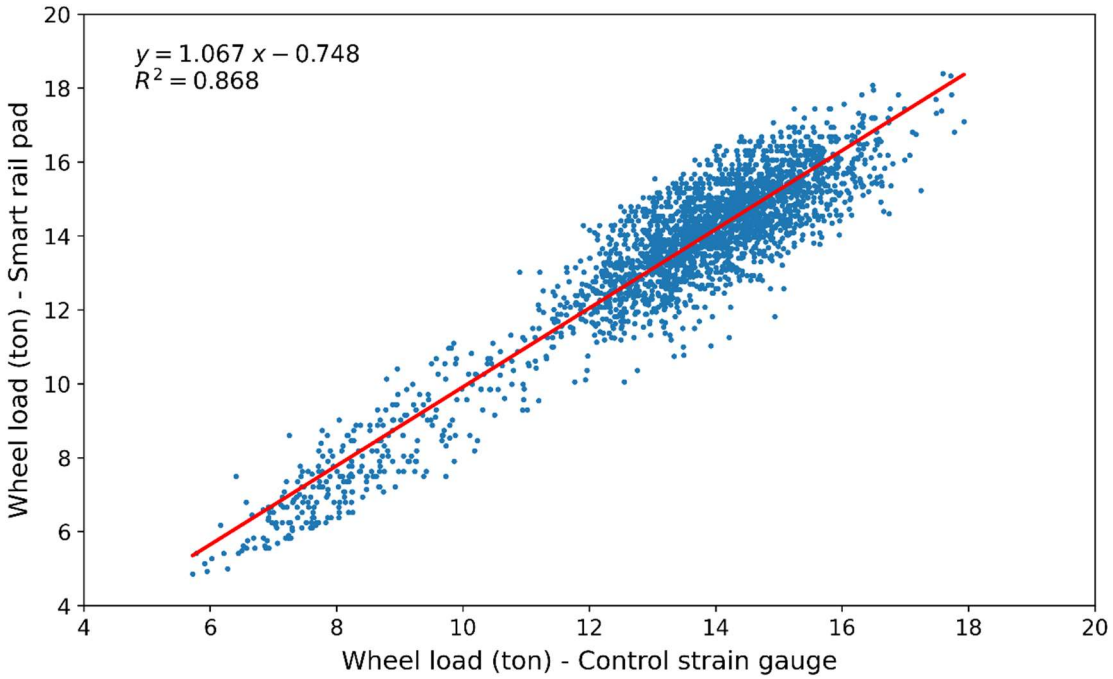

Figure 17: Linear relationship between the measured wheel loads and the true wheel loads

5 CONCLUSIONS

The following conclusions can be made with regard to the quantification of the dynamic response of a smart rail pad in both laboratory and field conditions:

- The smart rail pad was able to detect more than 60 % of the wheel defects on average as measured on an operational railway line. This is as accurate as expected because of the major limiting factor of the low sampling rate of the system when all three instruments are logging data. The strain gauge could also be used to detect wheel defects apart from the accelerometers.
- The smart rail pad showed excellent signal response to the variations in the loading of the tested trains and can be used to measure the corresponding wheel loads. The measured wheel loads were in close agreement with the control wheel loads with an average percent error of 6 %. The smart rail pad can be used for load sensing of wheel loads and as an axle counter.
- The smart rail pad can be used to quantify the condition of the train wheels to an acceptable degree by measuring accelerations and displacements to detect wheel defects. The smart rail pad can be used to estimate the wheel loads of those train wheels. The whole system can log the smart rail pad data automatically by detecting an oncoming train and switching the microcontroller into logging mode.

DECLARATION OF COMPETING INTEREST

The authors declare that they have no known competing financial interests or personal relationships that could have appeared to influence the work reported in this paper.

ACKNOWLEGDEMENTS

The authors gratefully acknowledge the assistance provided by the postgraduate students during the installation of the equipment at the field-testing site. The funding provided by Transnet Freight Rail towards the Chair in Railway Engineering is also gratefully acknowledged. Transnet Freight Rail is also thanked for allowing the site to be used for this research.

6 REFERENCES

ASTM Standard D638. (2014). *Standard Test Method for Tensile Properties of Plastics. ASTM International*, West Conshohocken, PA, 2014, DOI: 10.1520/D0638-14, <www.astm.org>.

ASTM Standard D695. (2015). *Standard Test Method for Compressive Properties of Rigid Plastics*. ASTM International, West Conshohocken, PA, 2015, DOI: 10.1520/D0695-15, <www.astm.org>.

Aursudkij, B., McDowell, G.R. and Collop, A. (2009). Cyclic loading of railway ballast under triaxial conditions and in a railway test facility. *Granular Matter*, Vol. 11, No. 6, pp 391-401.

Billauer, E. (2010). *Peak Detection in Python*. Online: https://gist.github.com/endolith/250860. Accessed 10 October 2021.

Eisenmann, J. (1972). Germans gain a better understanding of track structure. *Railway Gazette International*, Vol. 128, No. 8, pp 305-308.

Esveld, C. (2001). *Modern Railway Track*. 2nd Edition. MRT-Productions, Netherlands.

Gräbe, P.J., Clayton, C.R.I. and Shaw, F.J. (2005). Deformation measurement on a heavy haul track formation. In *Proceedings of 8th International Heavy Haul Conference*. International Heavy Haul Association, pp 287-295.

Hong, C., Yuan, Y., Yang, Y., Zhang, Y. and Abro, Z.A. (2019). A simple FBG pressure sensor fabricated using fused deposition modelling process. *Sensors and Actuators A: Physical*, Vol. 285, No. 1, pp 269-274.

Lee, H., Eom, R. and Lee, Y. (2019). Evaluation of the Mechanical Properties of Porous Thermoplastic Polyurethane Obtained by 3D Printing for Protective Gear. *Advances in Materials Science and Engineering*, Vol. 2019, article ID 5838361.

Milne, D., Le Pen, L., Watson, G., Thompson, D., Powrie, W., Hayward, M. and Morley, S. (2016). Proving MEMS Technologies for Smarter Railway Infrastructure. *Procedia Engineering*, Vol. 143, No. 1, pp 1077-1084.

Priest, J.A., Powrie, W., Yang, L., Gräbe, P.J. and Clayton, C.R.I. (2010). Measurements of transient ground movements below a ballasted railway line. *Géotechnique*, Vol. 60, No. 9, pp 667-677.

Profillidis, V. A. (2000). *Railway Engineering*. 2nd Edition. Ashgate Publishing Limited, United Kingdom.

Russel, E.J., Rose, J.G. and Clarke, D.B. (2020). In-Track Timber Crosstie-Ballast Interfacial Pressure Measurements for Revenue Freight Trains and DOTX 218/219 Test Train Operating Conditions. *In Proceedings of Railway Roadbed & Ballast Symposium*. RRB. pp 135-155.

Sol-Sánchez, M., Castillo-Mingorance, J.M., Moreno-Navarro, F., Mattinzioli, T. and Rubio-Gámez, M.C. (2021). Piezoelectric-sensored sustainable pads for smart railway traffic and track state monitoring: Full-scale laboratory tests. *Construction and Building Materials*, Vol. 301, No. 1, article no. 124324.

Sol-Sánchez, M., Castillo-Mingorance, J.M., Moreno-Navarro, F. and Rubio-Gámez, M.C. (2021). Smart rail pads for the continuous monitoring of sensored railway tracks: Sensors analysis. *Automation in Construction*, Vol. 132, No. 1, article no. 103950.

Stenström, C., Lindqvist, J. and Andersson, F. (2019). Condition based maintenance using MEMS accelerometers: For faster development of IoT in railways. In *Proceedings of the International Heavy Haul Association (IHHA) STS Conference*. International Heavy Haul Association (IHHA). Norway.

Thompson, D. (2009). *Railway Noise and Vibrations: Mechanisms, Modelling and means of control*. 1st Edition. Elsevier, United Kingdom.

Wang, J., Yang, B., Lin X., Gao, L., Liu, T., Lu, Y. and Wang, R. (2020). Research of TPU Materials for 3D Printing Aiming at Non-Pneumatic Tires by FDM Method. *Polymers*, Vol. 12, No. 11, article no. 2492.

Woschitz, H. (2011). Development of a rail-strain-pad using FBG sensors. *5th International Conference on Structural Health Monitoring of Intelligent Infrastructure (SHMII-5)*. Cancun, Mexico, Sunday 11th to Thursday 15th December 2011.

Zhang, S.L., Koh, C.G. and Kuang, K.S.C. (2014). Fibre Optic Rail Pad Sensor Based Wheel Flat Identification. *In Proceedings of the Second International Conference on Railway Technology: Research, Development and Maintenance*. Civil-Comp Press, Stirlingshire, UK, Paper 168.

Zhang, S.L., Koh, C.G. and Kuang, K.S.C. (2018). Proposed rail pad sensor for wheel-rail contact force monitoring. *Smart Materials and Structures*, Vol. 27, No. 11, article no. 115041.